Meriem Goudjil*, Giovanni Orazio Lepore, Paola Bonazzi, Djillali Mezaoui, Alessio Mezzi, Eleonora Bolli, Francesco Di Benedetto and Luca Bindi

A new layered potassium-based molybdenum–tungsten monophosphate: synthesis, crystal structure, XPS and magnetic studies

https://doi.org/10.1515/zkri-2023-0027
Received June 29, 2023; accepted August 1, 2023;
published online September 13, 2023

Abstract: A new compound, $K_5[(Mo_{3.2}W_{1.8})O_{11}](PO_4)_3[(P_{0.5}Mo_{0.5})O_4]$, was synthesized via solid-state reaction and its crystal structure was determined by single-crystal X-ray diffraction. This compound crystallizes in the space group *Pnma*, with a = 9.0360(4) Å, b = 10.1603(4) Å, c = 26.1538(12) Å and V = 2401.14(18) Å^3. The structure consists of a corner-sharing MO_6–TO_4 (M = Mo, W; T = P, Mo) polyhedral connection arranged to form an ordered packing of ~14.9 Å-thick layers parallel to (001). The stacking of the layers forms trigonal, tetragonal and hexagonal channels. XPS study reveals the presence of W at the hexavalent state only, whereas Mo appears as a mixed-valent species (Mo^{6+}, Mo^{5+} and Mo^{4+}). Magnetic susceptibility reveals the occurrence of a relevant antiferromagnetic coupling and is consistent with the presence of reduced metal species as indicated by the XPS results.

Keywords: crystal structure; magnetic susceptibility; mixed-valent molybdenum; molybdenum phosphate; synthesis; XPS

***Corresponding author: Meriem Goudjil**, Dipartimento di Scienze della Terra, Università degli Studi di Firenze, Via La Pira 4, Firenze I-50121, Italy; and Laboratoire des Sciences des Matériaux, Faculté de Chimie, Université des Sciences et de la Technologie Houari Boumediene, Bab Ezzouar, Alger 16111, Algeria, E-mail: meriem.goudjil@unifi.it. https://orcid.org/0000-0003-3401-4294

Giovanni Orazio Lepore, Paola Bonazzi and Luca Bindi, Dipartimento di Scienze della Terra, Università degli Studi di Firenze, Via La Pira 4, Firenze I-50121, Italy

Djillali Mezaoui, Laboratoire des Sciences des Matériaux, Faculté de Chimie, Université des Sciences et de la Technologie Houari Boumediene, Bab Ezzouar, Alger 16111, Algeria

Alessio Mezzi and Eleonora Bolli, Consiglio Nazionale delle Ricerche-Istituto per lo Studio di Materiali Nanostrutturati, CNR-ISMN, Via Salaria km 29.3, 00015 Monterotondo Stazione, Rome, Italy

Francesco Di Benedetto, Dipartimento di Fisica e Scienze della Terra, Università degli Studi di Ferrara, Via Giuseppe Saragat 1, Ferrara 44124, Italy

1 Introduction

Transition metal phosphates are compounds with fascinating architectures including monomers, chains, layers and three-dimensional frameworks [1–4]. Generally, their structures are characterized by a host-lattice that is constructed predominantly by PO_4 tetrahedra linked to other coordination polyhedra such as MO_4, MO_5 and MO_6 (M: transition metal with valence states ranging from +2 to +6) [5–10]. Consequently, a great number of compounds with different crystal structures can be envisioned both on the basis of a different polyhedral assemblage and/or incorporation of a variety of guest cations [11–13].

Molybdenum phosphates (MoPs) show various polyhedral connectivity with Mo in different oxidation states (Mo^{3+} [14], Mo^{4+} [15], Mo^{5+} [16] or Mo^{6+} [17, 18]) yielding to several structural types (e.g., polyoxometalates [19], tungsten bronzes [20, 21] and Nasicon [22]).

Mixed-valent MoPs are also reported as glasses (e.g., [23, 24]), thin films (e.g., [25]) and powder compounds (e.g., [26]); only few, occurring as single crystals, have been described from a structural point of view (e.g., Mo^{4+}/Mo^{5+} [27] and Mo^{5+}/Mo^{6+} [28–30]).

Over the past two decades, mixed-valent MoPs have gained an increasing interest as new cathode materials for lithium- and sodium-ion batteries [31–34], being considered as one of the promising candidates for affordable and scalable energy storage [35]. MoPs are also used as support in heterogeneous catalysis reactions [36–39]. MoPs with mixed-valent character also possess redox properties that make them potential catalysts for selective oxidation reactions (e.g., partial oxidation of propane to acrolein [40, 41], *n*-butane to maleic anhydride [42] and methanol to formaldehyde [36]).

With the aim to synthesize new mixed-valent transition-metal phosphates, we explored the system K–Mo(W)–P–O and obtained a new compound which is here characterized.

2 Experimental methods

2.1 Synthesis

The crystalline compound was prepared by a two steps solid-state process. In the first step, a mixture of K_2CO_3 (Merck, 99.0 %), MoO_3 (Honeywell Fluka, 99.5 %), WO_3 (Sigma Aldrich, 99.99 %) and $NH_4H_2PO_4$ (Merck, 99.99 %), in the molar ratios 3:5:2:4, was finely ground in an agate mortar and then left in a ceramic crucible over 2 h inside a furnace heated at 573 K in air. After complete evaporation of H_2O, CO_2 and NH_3, 1 mole of metallic Mo was added to the powder product and mixed thoroughly for 1 h, ideally yielding nominal formula $K_6Mo_6W_2P_4O_{34}$. The grounded powder was loaded in a silica tube and placed under a base pressure of 10^{-4} mbar to be torch sealed. The ampoule was then deposited in a tubular furnace heated at 833 K for 3 days to allow the crystal growth via vapour-phase transport process. The temperature gradient was 2.5 K/cm between the hot- and the cold-zones over a 10 cm long ampoule. After the chemical reaction took place, the temperature of the furnace was decreased at 60 K/h up to 473 K and finally quenched at room temperature.

Dark blue crystals (~20 mg with dimensions in the range 10–100 μm) formed in the cold zone of the ampoule, whereas a darker sintered powder was found in the hot zone. Moreover, the excess of the reagents was deposited as a black crust coating the internal wall of the reaction tube.

2.2 Chemical composition

Semi-quantitative chemical analysis was performed by means of Energy Dispersive X-ray Spectroscopy (EDS) on crystals dispersed on a carbon tape and covered with a 40 nm graphite layer (Figure S1-a) using a ZEISS EVO MA15 scanning electron microscope equipped with an OXFORD INCA micro-analyser, operating with an accelerating voltage of 20 KV, a current of 0.3 nA and a working distance of 10.0 mm.

The EDS analysis confirmed the presence of the intended elements (Figure S1-b). The chemical composition (average of 5 spots) of the crystal (belonging to the dark blue compounds) used for the structural study in molar ratios is: K: 0.334, P: 0.260, Mo: 0.261 and W: 0.144.

2.3 Single crystal X-ray diffraction

X-ray diffraction data were collected at room temperature (T = 293 K) on a dark blue crystal (hereafter K–MoWP) with an Oxford Diffraction Xcalibur 3 diffractometer, equipped with a graphite monochromatized Mo-$K\alpha$ (λ = 0.71073 Å) radiation and a Sapphire CCD detector. Dataset integration and empirical corrections were applied using the *CrysAlis PRO* software [43]. A total of 8344 reflections were collected, yielding 3960 independent reflections in the *mmm* Laue group (R_{int} = 0.062). Reflections conditions (0kl: $k + l = 2n + 1$ and $hk0$: $h = 2n + 1$) were consistent with both the space groups $Pn2_1a$ and *Pnma*. We attempted to solve the structure in both space groups. However, the final solution was successfully achieved in the centrosymmetric *Pnma* space group in accordance with the statistical test on the distribution of $|E|$ values ($|E^2 - 1|$ = 0.924).

Table 1: Summary of crystal data, intensity measurement and structure refinement parameters for $K_5[(Mo_{3.2}W_{1.8})O_{11}](PO_4)_3[(P_{0.5}Mo_{0.5})O_4]$.

Crystal data	
Chemical formula	$K_5[(Mo_{3.2}W_{1.8})O_{11}](PO_4)_3[(P_{0.5}Mo_{0.5})O_4]$
M_r	1427.98
Crystal system, space group	Orthorhombic, *Pnma* (no. 62)
Temperature (K)	293
Cell dimensions (Å)	a = 9.0360(4)
	b = 10.1603(4)
	c = 26.1538(12)
V (Å^3)	2401.14(18)
Z	4
Radiation type – λ (Å)	Mo $K\alpha$ – 0.71073
ρ_{calc} (g cm^{-3})	3.950
μ (mm^{-1})	11.88
Crystal size (mm^3)	0.06 × 0.08 × 0.10
Data collection	
θ range (°)	4.3–31.4
$F(000)$	2618
Index ranges	$-8 \le h \le 13$; $-14 \le k \le 11$; $-17 \le l \le 37$
No. of measured, independent and observed [$F > 4\sigma(F)$] reflections	8344, 3960, 2784
R_{int}	0.062
$(\sin\theta/\lambda)_{max}$ (Å^{-1})	0.744
Refinement	
$R[F > 4\sigma(F)]$, $wR(F^2)$, S	0.051, 0.078, 1.02
No. of reflections	3960
No. of parameters	209
Largest diff. peak and hole (e•Å^{-3})	−2.21; 2.23

The structure was solved by direct methods and then refined by least-squares fitting based on $|F^2|$ using the *SHELXTL* program [44]. Mo(W), P and K atoms were initially located, whereas oxygen atoms were found successively in the difference Fourier maps. Crystal data, data collection and structure refinement details are summarized in Table 1.

Scattering curves for neutral atoms were taken from the *International Tables of Crystallography* [45]. The occupancy of all the octahedral (M), tetrahedral (T) and K sites was refined (Mo vs. W, P vs. Mo and K vs. vacancy for M, T and K sites, respectively). K sites were found to be fully occupied by potassium and their occupancy was then fixed. In the final model, with anisotropic atomic displacement parameters for all the atoms and no constraints, the residual value settled at R = 5.1 % for 2784 independent observed reflections [4$\sigma(F)$ level] and 209 parameters, and at R = 8.9 % for all 3960 independent reflections.

Atomic coordinates, site occupancies and equivalent isotropic displacement parameters are given in Table 2. The anisotropic displacement parameters are listed in Table S1. Table S2 and Table 3 report the bond valence sums (calculated according to the parameters of Brown and Altermatt [46]) and bond distances (along with distortion parameters [47]), respectively. Further crystallographic data can be obtained from the CIF deposited in the Cambridge Crystallographic Data Centre, CCDC number: 2072198.

Table 2: Atoms, Wyckoff positions, atomic coordinates, equivalent isotropic displacement parameters (Å^2) and occupancy factors for $K_5[(Mo_{3.2}W_{1.8})O_{11}](PO_4)_3[(P_{0.5}Mo_{0.5})O_4]$.

Atom	Site	*x*	*y*	*z*	U_{eq}	Occ.
T1(P/Mo)	4*c*	0.49449(18)	0.750000	0.53699(6)	0.0132(5)	0.464(6)/0.536(6)
T2(P)	4*c*	0.5654(3)	0.250000	0.85057(11)	0.0079(6)	1
T3(P)	8*d*	0.2271(2)	−0.01875(19)	0.79401(8)	0.0098(4)	1
M1(Mo/W)	4*c*	0.67011(6)	0.250000	0.63978(2)	0.00835(17)	0.301(6)/0.699(6)
M2(Mo/W)	8*d*	0.08025(6)	−0.07075(4)	0.67519(2)	0.00842(15)	0.671(5)/0.329(5)
M3(Mo/W)	8*d*	0.78112(6)	−0.06836(5)	0.58257(2)	0.00925(17)	0.758(5)/0.242(5)
K1	4*c*	0.3850(3)	0.250000	0.73528(10)	0.0238(7)	1
K2	8*d*	0.3269(3)	0.06607(19)	0.57534(8)	0.0338(6)	1
K3	4*c*	−0.0493(3)	0.750000	0.79514(12)	0.0282(8)	1
K4	4*c*	0.4325(5)	0.250000	0.98440(14)	0.0515(11)	1
O1	8*d*	0.6953(6)	−0.0965(4)	0.6575(2)	0.0137(13)	1
O2	4*c*	0.8142(9)	0.750000	0.5785(3)	0.0145(18)	1
O3	4*c*	0.4793(9)	0.250000	0.6368(3)	0.0136(17)	1
O4	4*c*	0.6084(10)	0.250000	0.9055(3)	0.022(2)	1
O5	8*d*	0.1513(7)	−0.0882(5)	0.7490(2)	0.0159(13)	1
O6	8*d*	0.2510(7)	−0.1020(5)	0.6490(2)	0.0199(14)	1
O7	4*c*	0.0227(9)	0.750000	0.6819(3)	0.0119(17)	1
O8	8*d*	−0.1075(6)	−0.0131(5)	0.7175(2)	0.0153(13)	1
O9	8*d*	−0.0316(6)	−0.0448(4)	0.61660(19)	0.0124(12)	1
O10	8*d*	0.1306(6)	0.1281(5)	0.6782(2)	0.0145(13)	1
O11	8*d*	0.7112(7)	0.1145(5)	0.5969(2)	0.0178(14)	1
O12	8*d*	0.8332(7)	−0.0285(5)	0.5220(2)	0.0211(14)	1
O13	8*d*	0.6648(6)	0.1222(5)	0.7006(2)	0.0131(12)	1
O14	4*c*	0.3978(9)	0.250000	0.8422(3)	0.0175(19)	1
O15	8*d*	0.5639(7)	−0.1108(5)	0.5654(2)	0.0225(15)	1
O16	4*c*	0.5391(13)	0.750000	0.4788(4)	0.040(3)	1
O17	4*c*	0.3158(12)	0.750000	0.5439(4)	0.043(3)	1

2.4 Powder X-ray diffraction

The sintered powder deposited in the hot zone was examined using powder X-ray diffraction (PXRD) in the 2θ range 5–70° with a Bruker D8 ADVANCE diffractometer operating with monochromatized Cu-*K*α radiation (λ = 1.5406 Å) in θ–2θ scan, with a step size of 0.010° and a scanning rate of 0.5 s/point.

The comparison between the experimental diffraction pattern (Figure S3) and that calculated on the basis of the structural model obtained from single-crystal data (Table 2) revealed some non-matching peaks indicating the presence of modest amount of $K(MoO_2)(PO_4)$ (PDF 01-089-1570). The unit cell-parameters, peak shape (double-Voigt approach), zero error, phase fractions and background parameters (5 terms Chebychev background polynomial) were refined using Pawley method [48] (R_p = 9.20 %, R_{wp} = 12.54 %, and S = 2.84).

2.5 X-ray photoelectron spectroscopy (XPS)

The XPS experiment was carried out using an ESCALAB 250Xi spectrometer (Thermo Fisher Scientific–UK) equipped with a monochromatic Al-*K*α source ($h\nu$ = 1486.6 eV) and a six-channeltron as detection system. The apparatus works in an Ultra-High Vacuum (UHV) system, where the base pressure of the analysis chamber during the experiments was approximately 3.4×10^{-9} mbar. An amount of ~4 mg of dark blue crystals selected from the cold zone was ground in an agate mortar (grain size down to about 20/30 µm) and spread on a gold foil. Electric contact between the sample and the apparatus was ensured by a metallic clip. The binding energy (BE) scale was calibrated by positioning the Au $4f_{7/2}$ peak at BE = 84.0 eV with an accuracy of ±0.1 eV, while the spectra were collected at pass energy of 50 eV. In order to investigate the electronic structure of W and Mo, spectra were acquired in the 31–45 eV and 227–240 eV energy ranges. The detected area was 900×900 µm^2, which was successively reduced down to few hundreds of squared microns, in order to maximize the signal/background ratio from the sample. The coverage was sufficient to hide the Au signal from the underlying gold foil.

The experimental data were collected and processed by the Avantage v.5 software (Thermo Fisher Scientific–UK). Shirley background subtraction and mixed Lorentzian/Gaussian peak shape (30 %) were used for the peak fitting.

2.6 Magnetic susceptibility

Variable-temperature magnetic susceptibility measurements were recorded with a Superconducting QUantum Interference Device

Table 3: Bond distances (Å) and polyhedra distortion parameters in the structure of $K_5[(Mo_{3.2}W_{1.8})O_{11}](PO_4)_3[(P_{0.5}Mo_{0.5})O_4]$.

T1O$_4$		**T2O$_4$**		**T3O$_4$**	
T1–O15	1.716(6) × 2	T2–O4	1.487(9)	T3–O1^{ix}	1.521(5)
T1–O16	1.575(10)	T2–O10	1.565(5) × 2	T3–O5	1.533(6)
T1–O17	1.625(10)	T2–O14	1.530(9)	T3–O8^{ii}	1.526(6)
				T3–O13^{ix}	1.545(5)
<T1–O>	1.658(8)	<T2–O>	1.537(7)	<T3–O>	1.531(5)
λ	1.0026	λ	1.0025	λ	1.0005
σ^2	1.67	σ^2	10.45	σ^2	1.86
M1O$_6$		**M2O$_6$**		**M3O$_6$**	
M1–O3	1.726(8)	M2–O5	2.043(6)	M3–O1	2.127(5)
M1–O11	1.814(5) × 2	M2–O6	1.718(6)	M3–O2	1.8726(15)
M1–O13	2.054(5) × 2	M2–O7	1.902(2)	M3–O9^{iii}	1.927(5)
M1–O14^{ii}	2.111(8)	M2–O8	2.109(5)	M3–O11	1.998(5)
		M2–O9	1.854(5)	M3–O12	1.703(6)
		M2–O10	2.073(5)	M3–O15	2.059(6)
<M1–O>	1.929(6)	<M2–O>	1.949(5)	<M3–O>	1.948(5)
λ	1.0213	λ	1.0163	λ	1.0171
σ^2	53.82	σ^2	38.20	σ^2	41.37
K1–O3	2.712(8)	K2–O16^{vii}	2.638(8)	K3–O5^{v}	2.729(6)
K1–O14	2.799(8)	K2–O6	2.665(6)	K3–O5	2.729(6)
K1–O13^{ix}	2.908(6)	K2–O4^{ix}	2.765(7)	K3–O6^{xi}	2.765(6)
K1–O13^{x}	2.908(6)	K2–O16^{vii}	2.638(8)	K3–O6^{ix}	2.765(6)
K1–O8^{viii}	2.945(5)	K2–O6	2.665(6)	K3–O8	3.192(6)
K1–O8^{ii}	2.945(5)	K2–O4^{ix}	2.765(7)	K3–O1^{ix}	2.975(6)
K1–O13	2.983(6)			K3–O1^{xi}	2.975(6)
K1–O13^{i}	2.983(6)			K3–O7	3.031(8)
K1–O10	3.007(6)			K3–O8^{v}	3.192(6)
K1–O10^{i}	3.007(6)				
K4–O4	2.606(9)				
K4–O17^{xii}	2.731(12)				
K4–O12^{ix}	2.973(6)				
K4–O12^{x}	2.973(6)				
K4–O11^{ix}	3.228(7)				
K4–O11^{x}	3.228(7)				
K4–O12^{xiii}	3.242(7)				
K4–O12^{xiv}	3.242(7)				

Symmetry codes are: (i) $x, -y + 1/2, z$; (ii) $x + 1/2, y, -z + 3/2$; (iii) $x + 1, y, z$; (iv) $-x + 3/2, -y, z-1/2$; (v) $x, -y-1/2, z$; (vi) $-x + 1, y-1/2, -z + 1$; (vii) $-x + 1, -y, -z + 1$; (viii) $x + 1/2, -y + 1/2, -z + 3/2$; (ix) $x-1/2, y, -z + 3/2$; (x) $x-1/2, -y + 1/2, -z + 3/2$; (xi) $x-1/2, -y-1/2, -z + 3/2$; (xii) $-x + 1/2, -y, z + 1/2$; (xiii) $-x + 3/2, y + 1/2, z + 1/2$; (xiv) $-x + 3/2, -y, z + 1/2$; (xv) $x-1, y, z$; (xvi) $-x + 1/2, -y, z-1/2$.

(SQUID) susceptometer (MPMS Quantum Design) in the temperature range 10–300 K at an applied magnetic field of 1.0 T. Measurements were performed on finely ground powder sample (deposited in the hot-zone of the reaction tube): 69.2 mg were used for the investigation. Magnetic data were corrected for the sample holder and diamagnetic contribution estimated from Pascal's constants [49]. Least-squares fitting of the experimental curves was done with the Curie–Weiss equation.

3 Results and discussion

3.1 Crystal structure description

The crystal-chemical formula of K–MoWP derived from the structural refinement, in good agreement with EDS data, is $K_5[(Mo_{3.2}W_{1.8})O_{11}](PO_4)_3[(P_{0.5}Mo_{0.5})O_4]$, whose charge balance requires that a small amount of the transition-metal cations is not hexavalent. This compound crystallizes in the *Pnma* space group with a novel crystal structure. The asymmetric unit includes three octahedral sites (M1, M2 and M3), three tetrahedral sites (T1, T2 and T3) and four high-coordinated sites (K1, K2, K3 and K4). As shown in Figure 1, corner-sharing MO_6-TO_4 chains running along [010] are arranged to form complex bundles having elliptic sections where K^+ cations are hosted. The major axes of the elliptic sections are oriented along [201] (blue) and along [–201] (red) and appear as a herringbone packing when projected down [010]. The projection along [100] (Figure 2) shows an ordered packing of ~14.9 Å-thick polyhedral layers related to each other through the *a*-glide plane perpendicular to [001]. The polyhedral connection inside the layers results in trigonal, tetragonal and two different types of hexagonal channels.

T2 and T3 are fully occupied by P and show typical average ^{IV}P–O distances (1.537 and 1.531 Å, respectively). On the other hand, the refined site scattering at the T1 site yields a mean electron number of 29.5 and a bond-valence sum of

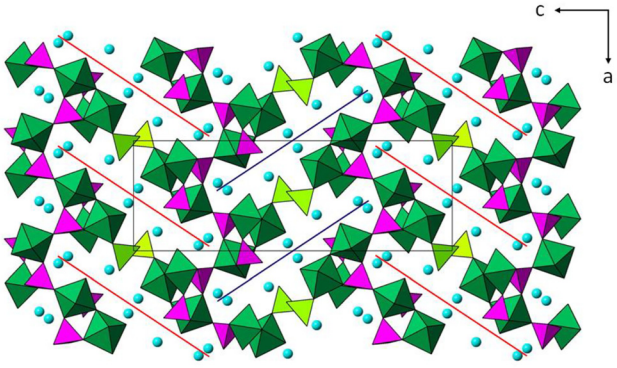

Figure 1: Polyhedral representation of the structure of $K_5[(Mo_{3.2}W_{1.8})O_{11}](PO_4)_3[(P_{0.5}Mo_{0.5})O_4]$ along the *b*-axis. The projection shows elliptic sections with major axes oriented along [201] (blue) and along [–201] (red), adopting a herringbone packing. Note that the extremities of the polyhedral bundles (light-green tetrahedra) are far apart along the *b*-axis (see Figure 2). Green: MO_6 octahedra, light-green: $T1O_4$ tetrahedra, pink: $T2O_4$ and $T3O_4$ tetrahedra, light blue spheres: K^+. Oxygen atoms are omitted for clarity.

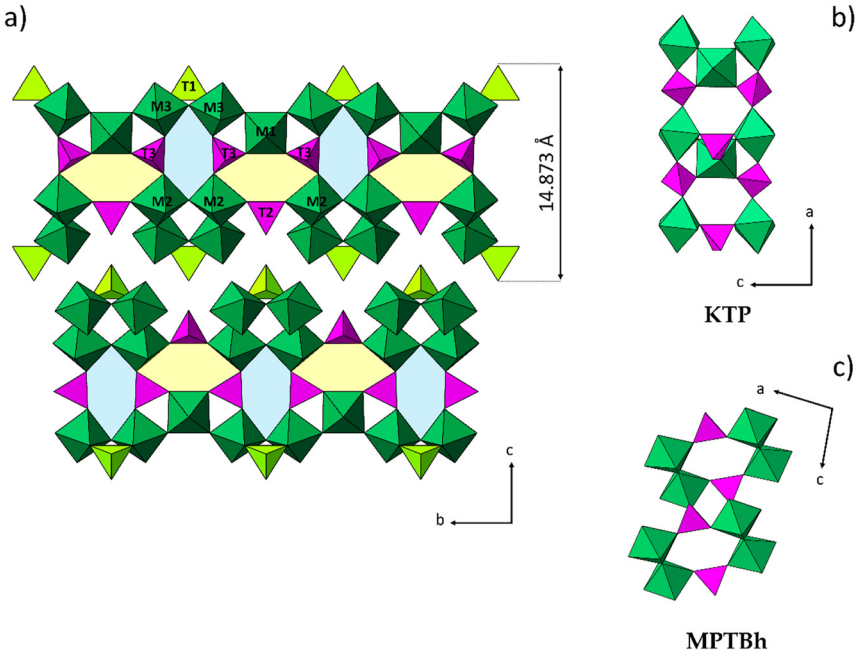

Figure 2: Structural sketch of $K_5[(Mo_{3.2}W_{1.8})O_{11}](PO_4)_3[(P_{0.5}Mo_{0.5})O_4]$: a) view along [100] showing a layered packing along the *c*-axis. This view shows a repeating sequence of two types of pseudo-hexagonal channels along the *b*-axis. In the first type (yellow), the polyhedral connection leads to pseudo-hexagonal channels of the type potassium titanium phosphate $KTiPO_5$ (KTP). In the second one (blue), the polyhedra are assembled to form pseudo-hexagonal channels similar to those observed in the monophosphate tungsten bronzes with hexagonal channels (MPTBh). Fragments of the KTP b) and MPTBh c) crystal structures projected along [010]. K and O atoms are omitted for clarity.

5.51 v.u. indicating the presence of a heavier, high-valent cation tentatively corresponding to either about 0.50 Mo^{6+} (ionic radius 0.41 Å [50]) or 0.25 W^{6+} (ionic radius 0.42 Å [50]) substituting for P. However, the <T1–O> distance (1.658 Å) fits better with 50 % incorporation of Mo^{6+} rather than 25 % W^{6+}. Despite the difference in size between Mo^{6+} and P^{5+}, no evidence of splitting of either T1 or the coordinated oxygen atoms was observed on the ΔF Fourier map. Nonetheless, some positional disorder can be inferred by the large anisotropic displacement parameters of O16 and O17, which are not shared with any octahedral cation (Table S1, Figure S2). The P ↔ Mo substitution has been observed earlier in the langbeinite-related structures $K_2M^{3+}{}_2(PO_4)_2(MoO_4)$ where P^{5+} and Mo^{6+} coexist in the 2:1 ratio in a tetrahedron exhibiting a mean bond distance of 1.58 Å [51].

M1, M2 and M3 octahedra are occupied by molybdenum and tungsten with variable proportions (Table 2). All MO_6 octahedra are rather distorted, as indicated by the wide range of variation in bond distances and distortion parameters (see Table 3). According to Domengès et al. [52], the spread of M–O bonds in W-bronzes is ascribed to the corner sharing between M-octahedra and PO_4-tetrahedra, leading to a lengthening of the P–O–M linkage. Therefore, the higher the positive charge in the octahedron, the stronger the distortion. Thus, the highest quadratic elongation (λ) value shown by M1 suggests that hexavalent cations are mainly ordered at this site. Accordingly, M1 is the smallest octahedron in the structure (<M1–O> = 1.929 Å). On the other hand, the lower λ values of M2 and M3 (see Table 3), associated with longer mean bond distances [<M2–O> = 1.949; <M3–O> = 1.948 Å], could be explained by the presence of lower-valence cations. The local MO_6 environments and bond lengths are shown in Figure 3.

The coordination spheres of potassium cations depicted in Figure S2 were determined on the basis of the maximum gap of K–O distances. K1 displays a 10-fold coordination with bond distances in the range 2.712(8)–3.007(6) Å. K2 is surrounded by 6 oxygen atoms with distances ranging from 2.638(8) to 2.952(6) Å; however, taking into account the threshold value (3.33 Å) suggested by Donnay and Allmann [53] for K–O bonds, two additional bonds [K2–O10 = 3.285(6) and K2–O17 = 3.316(4) Å] lead to a 6+2 coordination. K3 and K4 have 9- and 10-fold coordination, respectively, with bond lengths ranging between 2.729(6)–3.192(6) Å and 2.606(9)–3.242(7) Å.

3.2 XPS characterization

The neutrality of $K_5[(Mo_{3.2}W_{1.8})O_{11}](PO_4)_3[(P_{0.5}Mo_{0.5})O_4]$ requires a total positive charge of 31.5 for 5.5 (Mo, W) atoms p.f.u., thus implying a mixed-valence state for Mo and/or W (mean oxidation number of +5.73). XPS measurements show the spin orbit splitting characteristic of Mo 3*d* (Mo $3d_{3/2}$–Mo $3d_{5/2}$ in Figure 4a) and W 4*f* levels (W $4f_{5/2}$–W $4f_{7/2}$ in Figure 4b). Mo 3*d* and W 4*f* spectrum structure can be deconvoluted by means of multi-curve fitting. Shirley

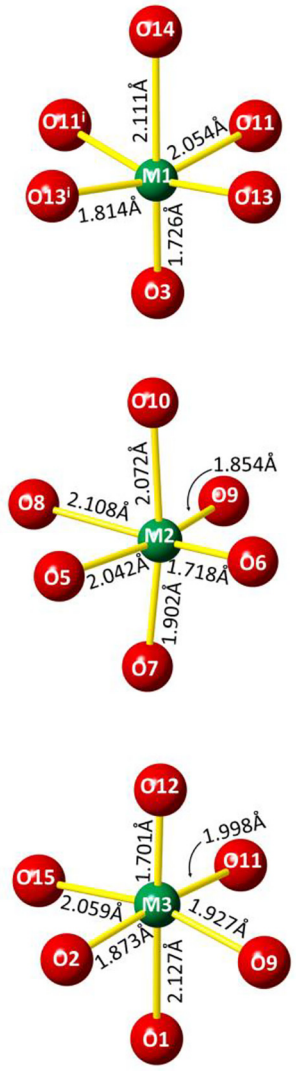

Figure 3: MO_6 octahedra environments and bond lengths.

background subtraction and mixed Lorentzian/Gaussian (Voigt) peak shape (30 %) were used for the peak fitting. The best fit for molybdenum was obtained by considering 6 fitting curves, i.e. three different doublets which can be connected to the presence of a different oxidation state for Mo [54, 55]: (*i*) 229.0 (Mo $3d_{5/2}$) and 232.1 eV (Mo $3d_{3/2}$) (Mo^{4+}, green line in Figure 4a); (*ii*) 231.5 and 234.6 eV (Mo^{5+}, blue); (*iii*) 232.7 and 235.8 eV (Mo^{6+}, orange). The identification of the various oxidation states was accomplished by measuring the relative shift of the Mo 3*d* core level peaks with respect to the non-reduced (Mo^{6+}) form, obtaining a good agreement with the values available in literature [56]. The relative abundance of the three oxidation states estimated on the basis of the proportion among the areas of the three components are 64 % (±6) for Mo^{6+}, 30 % (±3) for Mo^{5+} and 6 % (±1) for Mo^{4+}. Given the surficial character of the technique (up to a maximum of 5 nm in depth), the information on Mo oxidation states obtained from XPS might not be representative of the Mo speciation in the bulk; nonetheless, the presence of Mo^{5+} and Mo^{4+} even on the surface of the grains indicates that a significant amount of Mo must be present at its penta- and/or tetra-valent state also in the bulk. Tungsten W 4*f* core level spectrum was fitted by one doublet with peaks positioned at 35.3 eV (W $f_{7/2}$) and 37.4 eV (W $f_{5/2}$) (Figure 4b). The overlapped contributions arising from W 5*p*, Mo 4*p* and K 3*s* were properly considered. The doublet was ascribed to W^{6+} [57], and no reduced tungsten species was observed.

3.3 Magnetic properties

The evolution of the molar susceptibility (χ_m) and its reciprocal curve (χ_m^{-1}) versus temperature obtained upon analysis of the powder sample is shown in Figure 5. The data exhibit a conventional linear behaviour in the high-temperature regime (150–300 K), whereas the apparent deviation from the linearity observed at $T < 150$ K marks the occurrence of relevant antiferromagnetic (AF) interactions among paramagnetic ions.

The high-temperature regime was modelled through a linear regression with the law $\chi_m = C_M/(T - \theta)$, to obtain an esteem of the Curie (C_M) and Weiss (θ) constant values. C_M and θ values were determined to be 0.236 emu·K·mol^{-1} and −321 K, respectively. The effective magnetic moment, μ_{eff}, calculated from the Curie constant above 150 K is 1.37 μ_B. From these experimental evidences, the presence of an aliquot of low-valent molybdenum ions can be inferred. Since the second phase, $K(MoO_2)(PO_4)$, revealed by the XRPD investigation of the bulk microcrystalline powder, is diamagnetic (Mo ions are uniquely hexavalent d^0) as reported by Lsnyak et al. [58], the paramagnetic ions reasonably result only from the K–MoWP phase.

The negative and relatively high value [59, 60] of the Weiss constant suggests the occurrence of relevant antiferromagnetic interactions among neighbouring paramagnetic ions. This latter indication is compatible with the occurrence of reduced Mo species (e.g., Mo^{5+}, Mo^{4+} as revealed by XPS) in neighbouring M sites. Also the non-linear trend of the χ^{-1} shown in the inset to Figure 5 is attributable to the occurrence of local AF coupling among neighbouring paramagnetic species (via exchange or super-exchange interactions), as e.g. in diluted magnetic semiconductors [61].

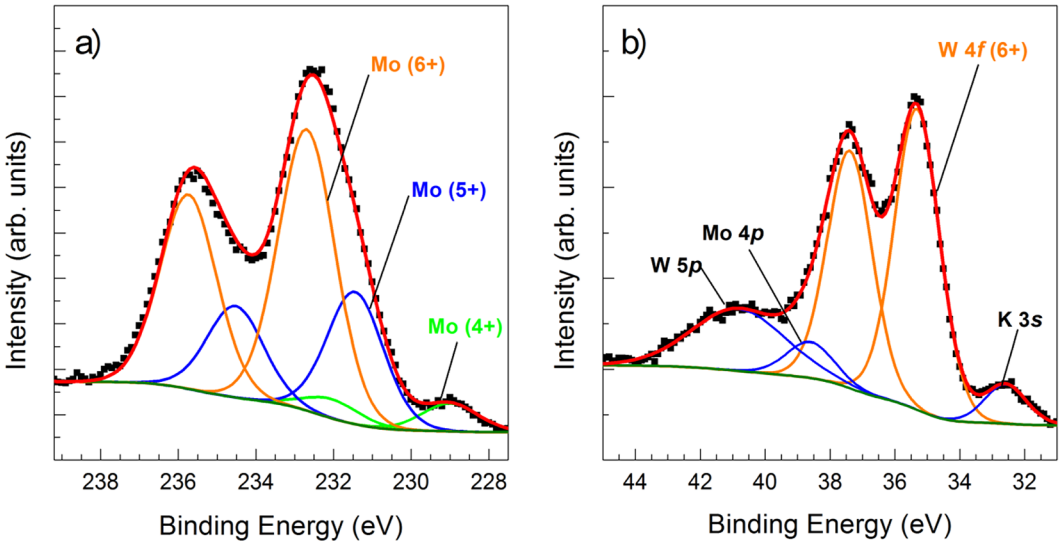

Figure 4: High resolution XPS core level spectrum of Mo 3*d* a) and W 4*f* b) levels and their spin orbit splitting. The curve fitting of the spin orbit doublets are traced in different colours. Background subtraction is also indicated. a) Molybdenum is present in three different oxidation states (6+, 5+ and 4+), whose peak area was 19,495 CPS × eV, 9174 CPS × eV and 1938 CPS × eV, respectively. For each doublet, only the Mo $3d_{5/2}$ component is marked by a label. b) Tungsten was detected uniquely in its (6+) oxidation state (only doublet W $f_{5/2}$–W $f_{7/2}$ is visible). The overlapped contributions arising from W 5*p*, Mo 4*p* and K 3*s* are also indicated. See text for the list of peak centre positions and energy difference of doublets.

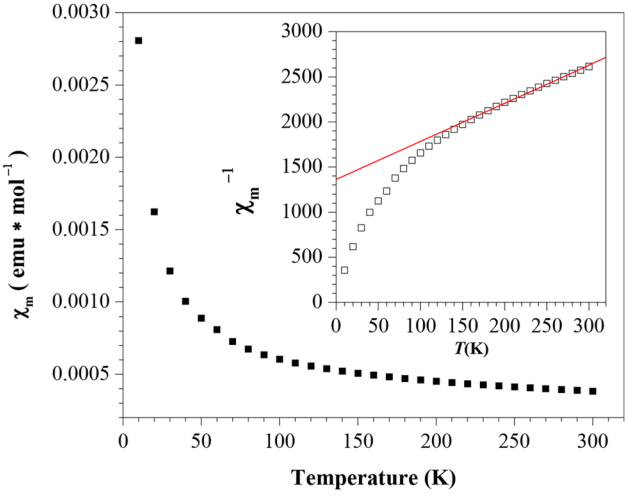

Figure 5: Magnetic susceptibility data as function of temperature for the molybdenum phosphate compound, Curie–Weiss fit (inset) with Curie constant C_M = 0.236 emu·K·mol^{-1} (effective moment, μ_{eff} = 1.37 μ_B) and Weiss constant θ = –321 K.

3.4 Relationships with other structural types

The view of the crystal structure along [100] depicted in Figure 2 shows a repeating sequence of two types of pseudo-hexagonal channels along the *b*-axis. The first type (yellow in Figure 2), with mean diameter of 5.00 Å, resembles those found in potassium titanium phosphate $KTiPO_5$ (KTP [62], see Figure 2a), although the linkage along [001] in K–MoWP is interrupted by missing tetrahedral sites, thus determining a layered packing. Thus, the stoichiometry of the KTP-like slab is $[KMP_{2/3}O_5]$. It is worth mentioning that in the KTP structure, TiO_6 octahedra are linked via common oxygen vertices forming *cis-trans* helical chains. Furthermore, only *cis*-linkage of the metal-oxygen chains is detected for KTP closely related structures, such as $K_2NiWO_2(PO_4)_2$ [63], $K_2MgWO_2(PO_4)_2$ [64] and $KM^{II}_{0.33}Nb_{0.67}PO_5$ (M^{II}: Mn, Co) [65]. In contrast, the framework of K–MoWP presents dissimilarity in the linkage of the MO_6 octahedral chains that follows a complex *cis-cis-trans* principle. In the second type of hexagonal channels (blue in Figure 2a), having a mean diameter of 4.96 Å, the polyhedral assemblage is similar to that observed in the monophosphate tungsten bronzes with hexagonal channels (MPTBh [66], as shown in Figure 2b).

4 Conclusions

The new K–MoWP compound, synthesized via vapour phase transport, exhibits a layered crystal structure based on octahedra (Mo, W) and tetrahedra (P, Mo) sharing their corners and generating wide cavities where K^+ ions are located.

XPS and magnetic susceptibility measurements, together with charge balance requirements, indicate the presence of a mixed-valent character for Mo (i.e. 6+, 5+ and 4+) ions whereas W occurs uniquely in 6+ oxidation state.

This is also in agreement with what expected from the synthesis method where metallic Mo^0 was added to other $M^{6+}O_3$ oxidized components.

According to the structure refinement results, the total number of Mo (in all its oxidation states) and W is 3.7 and 1.8 (apfu.), respectively. Assuming that tetrahedral Mo is hexavalent only, the resulting average Mo valence in octahedral sites must be about 5.5. If we tentatively extrapolate the XPS results to the whole bulk material, the following formula for K–MoWP can be proposed: $K_5[(Mo^{6+}_{1.9}Mo^{5+}_{1.1}Mo^{4+}_{0.2}W^{6+}_{1.8})O_{11}](PO_4)_3[(Mo^{6+}_{0.5}P_{0.5})O_4]$.

This compound exhibits both mixed occupancy (Mo, W) and mixed valence (Mo^{6+}, Mo^{5+}, and Mo^{4+}) in octahedral sites; the occurrence of similar conditions has also been observed in Mo/W mixed-oxides [67, 68]. Mo–W bronzes showing these characteristics can be seen as paradigmatic structures for the study of the absorption optical properties related to the presence of *homo*/*hetero*-charge transfer phenomena in intervalence systems (IVCT: intervalence charge transfer).

Acknowledgements: The authors thank Centro di Servizi di Microscopia Elettronica e Microanalisi (MEMA), University of Florence (Italy) where EDS analysis was performed and Centro di Cristallografia Strutturale (CRIST), University of Florence where X-ray powder and single-crystal diffraction measurements were carried out. The authors express their warmest thanks to Andrea Caneschi (DIEF, University of Florence) for having performed the SQUID measurements. M.G. thanks deeply Dr. Saulius Kaciulis (CNR-ISMN of Roma) for his advices and for the fruitful discussion while performing XPS experiments.

Author contributions: All the authors have accepted responsibility for the entire content of this submitted manuscript and approved submission.

Competing interests: The authors declare that they have no known competing financial interests or personal relationships that could have appeared to influence the work reported in this paper.

Research funding: The present work was funded by MIUR-PRIN2017, project "TEOREM Deciphering geological processes using Terrestrial and Extra-terrestrial ORE Minerals", [prot. 2017AK8C32], PI: Luca Bindi.

References

1. Alberti G., Casciola M., Costantino U., Vivani R. Layered and pillared metal (IV) phosphates and phosphonates. *Adv. Mater*. 1996, *8*, 291–303.
2. Cheetham A. K., Férey G., Loiseau T. Open-framework inorganic materials. *Angew. Chem. Int. Ed.* 1999, *38*, 3268–3292.
3. Natarajan S. Hydrothermal synthesis and structures of two zero-dimensional zinc phosphate polymorphs. *Solid State Sci.* 2005, *7*, 1542–1548.
4. Natarajan S., Mandal S. Open–framework structures of transition-metal compounds. *Angew. Chem. Int. Ed.* 2008, *47*, 4798–4828.
5. Shao Y., Xiao X., Zhu Y. P., Ma T. Y. Single-crystal cobalt phosphate nanosheets for biomimetic oxygen evolution in neutral electrolytes. *Angew. Chem. Int. Ed.* 2019, *58*, 14599–14604.
6. Zhao Z., Chen H., Xiang H., Dai F.-Z., Wang X., Peng Z., Zhou Y. $(La_{0.2}Ce_{0.2}Nd_{0.2}Sm_{0.2}Eu_{0.2})PO_4$: a high-entropy rare-earth phosphate monazite ceramic with low thermal conductivity and good compatibility with Al_2O_3. *J. Mater. Sci. Technol.* 2019, *35*, 2892–2896.
7. Qi J., Lin Y. P., Chen D., Zhou T., Zhang W., Cao R. Autologous cobalt phosphates with modulated coordination sites for electrocatalytic water oxidation. *Angew. Chem.* 2020, *132*, 9002–9006.
8. Zhao H., Yuan Z. Y. Insights into transition metal phosphate materials for efficient electrocatalysis. *ChemCatChem* 2020, *12*, 3797–3810.
9. Guo J., Tudi A., Han S., Yang Z., Pan S. Sn_2PO_4I: an excellent birefringent material with giant optical anisotropy in non π-conjugated phosphate. *Angew. Chem. Int. Ed.* 2021, *60*, 24901–24904.
10. Karafiludis S., Buzanich A. G., Kochovski Z., Feldmann I., Emmerling F., Stawski T. M. Ni- and Co-struvites: revealing crystallization mechanisms and crystal engineering toward applicational use of transition metal phosphates. *Cryst. Growth Des.* 2022, *22*, 4305–4315.
11. Chihara K., Katogi A., Kubota K., Komaba S. $KVPO_4F$ and $KVOPO_4$ toward 4 volt-class potassium-ion batteries. *Chem. Commun.* 2017, *53*, 5208–5211.
12. Colodrero R. M., Olivera-Pastor P., Cabeza A., Bazaga-García M. Properties and applications of metal phosphates and pyrophosphates as proton conductors. *Materials* 2022, *15*, 1292.
13. Mighri Z., Souiwa K., Rostas A. M., Patru R. E., Bocirnea A. E., Iacob N., Kuncser V., El Khouja O., Leonat L. N., Hidouri M., Nasri H., Galca A. C. Structural and electrical properties of novel Cr/Fe mixed transition-metal phosphates. *Inorg. Chem.* 2023, *62*, 8530–8542.
14. Leclaire A., Chardon J., Borel M., Grandin A., Raveau B. A new molybdenum (III) phosphate: $BaMo_2P_4O_{14}$ isotypic with $BaM_2P_4O_{14}$ ($M = Ti^{III}$, V^{III}). *Z. Anorg. Allg. Chem*. 1992, *617*, 127–130.
15. Leclaire A., Chardon J., Raveau B. A new lead Mo (IV) phosphate with a tunnel structure: $Pb_2Mo_2O(PO_4)_2P_2O_7$. *J. Solid State Chem.* 2003, *172*, 412–416.
16. Leclaire A., Borei M. M., Grandin A., Raveau B. A novel form of molybdenum (V) phosphate: δ-$KMo_2P_3O_{13}$. *Z. Kristallogr.* 1989, *188*, 77–84.
17. Luo S., Kang L., Lin Z., Chen C. K_3MoPO_7: the first molybdenum phosphate with edge-sharing MoO_6 octahedra and PO_4 tetrahedra. *RSC Adv.* 2014, *4*, 27122–27125.
18. Liu H., Wu H., Yu H., Hu Z., Wang J., Wu Y. Effect of Mo/P ratios on dimensions: syntheses, structures, and properties of three new molybdophosphates. *Inorg. Chem.* 2020, *59*, 5742–5750.
19. Yu K., Zhou B.-B., Yu Y., Su Z.-H., Wang H.-Y., Wang C.-M., Wang C.-X. Influence of pH and organic ligands on the supramolecular network based on molybdenum phosphate/strontium chemistry. *Dalton Trans*. 2012, *41*, 10014–10020.
20. Ledain S., Leclaire A., Borel M., Provost J., Raveau B. A monophosphate molybdenum bronze built up from ReO_3-type slabs: $Ag_{0.7}Mo_3O_7(PO_4)$. *J. Solid State Chem.* 1998, *140*, 128–133.
21. Roussel P., Pérez O., Labbé P. Phosphate tungsten bronze series: crystallographic and structural properties of low-dimensional conductors. *Acta Crystallogr. B Struct. Sci.* 2001, *57*, 603–632.
22. Panin R. V., Drozhzhin O. A., Fedotov S. S., Khasanova N. R., Antipov E. V. NASICON-type $NaMo_2(PO_4)_3$: electrochemical activity of

the Mo^{4+} polyanion compound in Na-cell. *Electrochim. Acta* 2018, *289*, 168–174.
23. El-Batal A., Saeed A., Hendawy N., El-Okr M., El-Mansy M. Influence of Mo or/and Co ions on the structural and optical properties of phosphate zinc lithium glasses. *J. Non-Cryst. Solids* 2021, *559*, 120678.
24. Renka S., Pavić L., Tricot G., Mošner P., Koudelka L., Moguš-Milanković A., Šantić A. A significant enhancement of sodium ion conductivity in phosphate glasses by addition of WO_3 and MoO_3: the effect of mixed conventional–conditional glass-forming oxides. *Phys. Chem. Chem. Phys.* 2021, *23*, 9761–9772.
25. Watson I., Connor J. A., Whyman R. Non-crystalline chromium, molybdenum and tungsten phosphate films prepared by metal organic chemical vapour deposition. *Thin Solid Films* 1991, *201*, 337–349.
26. Ren J.-T., Chen L., Wang H.-Y., Yuan Z.-Y. Aqueous Al-N_2 battery assembled by hollow molybdenum phosphate microspheres for simultaneous NH_3 production and power generation. *J. Chem. Eng.* 2021, *418*, 129447.
27. Wen B., Liu J., Chernova N. A., Wang X., Janssen Y., Omenya F., Khalifah P. G., Whittingham M. S. $Li_3Mo_4P_5O_{24}$: a two-electron cathode for lithium-ion batteries with three-dimensional diffusion pathways. *Chem. Mater.* 2016, *28*, 2229–2235.
28. Borel M., Guesdon A., Leclaire A., Grandin A., Raveau B. New mixed-valent molybdenum monophosphates with the $KMo_3P_2O_{14}$ structure. *Z. Anorg. Allg. Chem*. 1994, *620*, 569–573.
29. Ledain S., Leclaire A., Borel M., Provost J., Raveau B. A mixed valent molybdenum monophosphate with a bidimensional connection of MoO_6 octahedra: $Li_3Mo_3O_5(PO_4)_3$. *J. Solid State Chem.* 1997, *133*, 391–399.
30. Zhang S., Lu Y., Sun X.-W., Li Z., Dang T.-Y., Zhang Z., Tian H.-R., Liu S.-X. Purely inorganic frameworks based on polyoxometalate clusters with abundant phosphate groups: single-crystal to single-crystal structural transformation and remarkable proton conduction. *Chem. Commun.* 2020, *56*, 391–394.
31. Uebou Y., Okada S., Yamaki J.-I. Electrochemical insertion of lithium and sodium into $(MoO_2)_2P_2O_7$. *J. Power Sources* 2003, *115*, 119–124.
32. Wen B., Chernova N. A., Zhang R., Wang Q., Omenya F., Fang J., Whittingham M. S. Layered molybdenum (oxy) pyrophosphate as cathode for lithium-ion batteries. *Chem. Mater.* 2013, *25*, 3513–3521.
33. Deng W., Feng X., Xiao Y., Li C. Layered molybdenum (oxy) pyrophosphate $(MoO_2)_2P_2O_7$ as a cathode material for sodium-ion batteries. *ChemElectroChem* 2018, *5*, 1032–1036.
34. Dai S., Feng T., Chen C., Li X., Wu M. Communication–phosphate $K(Mo_2PO_6)(P_2O_7)$ as a novel cathode material for potassium ion batteries: structure and electrochemical properties. *J. Electrochem. Soc.* 2020, *167*, 110517.
35. Qin Z., Song Y., Liu Y., Liu X.-X. Accessing the proton storage in neutral buffer electrolytes using an electrodeposited molybdenum phosphate. *Energy Storage Mater.* 2022, *53*, 569–579.
36. Whiting G. T., Bartley J. K., Dummer N. F., Hutchings G. J., Taylor S. H. Vanadium promoted molybdenum phosphate catalysts for the vapour phase partial oxidation of methanol to formaldehyde. *Appl. Catal. A* 2014, *485*, 51–57.
37. Zhang X., Zhang Z., Wu D., Zhao X., Zhou Z. $K_{1-x}Mo_3P_2O_{14}$ as support for single-atom catalysts. *J. Phys. Chem. C* 2017, *121*, 22895–22900.
38. Gadamsetti S., Mathangi N., Hussain S., Velisoju V. K., Chary K. V. Vapor phase esterification of levulinic acid catalyzed by γ-Al_2O_3 supported molybdenum phosphate catalysts. *Mol. Catal.* 2018, *451*, 192–199.
39. Rawat S., Gupta P., Singh B., Bhaskar T., Natte K., Narani A. Molybdenum-catalyzed oxidative depolymerization of alkali lignin: selective production of Vanillin. *Appl. Catal. A* 2020, *598*, 117567.
40. Zhang X., Wan H.-L., Weng W.-Z., Yi X.-D. Effect of promoter Ce on silver-molybdenum-phosphate catalysts for selective oxidation of propane to acrolein. *J. Mol. Catal. A: Chem.* 2003, *200*, 291–300.
41. Zhang X., Wan H.-L., Weng W.-Z., Yi X.-D. Effect of Ag promoter on redox properties and catalytic performance of Ag–Mo–PO catalysts for oxidative dehydrogenation of propane. *Appl. Surf. Sci.* 2003, *220*, 117–124.
42. Pierini B. T., Lombardo E. A. Cr, Mo and W used as VPO promoters in the partial oxidation of n-butane to maleic anhydride. *Catal. Today* 2005, *107*, 323–329.
43. Agilent. *CrysAlis PRO*; Agilent Technologies Ltd: Yarnton, Oxfordshire, England, 2014.
44. Sheldrick G. M. SHELXT: integrating space group determination and structure solution. *Acta Crystallogr. A Found. Adv.* 2014, *70*, C1437.
45. Wilson A. J. C., Geist V. *International Tables for Crystallography. Volume C: Mathematical, Physical and Chemical Tables*; Kluwer Academic Publishers: Dordrecht/Boston/London, 1992. (published for the International Union of Crystallography), 883 Seiten. 1993, Wiley Online Library.
46. Brown I., Altermatt D. Bond-valence parameters obtained from a systematic analysis of the inorganic crystal structure database. *Acta Crystallogr. Sect. B: Struct. Sci.* 1985, *41*, 244–247.
47. Robinson K., Gibbs G., Ribbe P. Quadratic elongation: a quantitative measure of distortion in coordination polyhedra. *Science* 1971, *172*, 567–570.
48. Pawley G. Unit-cell refinement from powder diffraction scans. *J. Appl. Crystallogr.* 1981, *14*, 357–361.
49. O'Connor C. *Magnetochemistry: Advances in Theory and Experimentation*; Lippard S. J., Ed., vol. 29. Massachusetts Institute of Technology: Massachusetts, 1982; pp. 203–283.
50. Shannon R. D. Revised effective ionic radii and systematic studies of interatomic distances in halides and chalcogenides. *Acta Crystallogr. A Cryst. Phys., Diffr., Theor. Gen. Crystallogr.* 1976, *32*, 751–767.
51. Slobodyanik N. S., Terebilenko K. V., Ogorodnyk I. V., Zatovsky I. V., Seredyuk M., Baumer V. N., Gütlich P. $K_2M^{III}{}_2(M^{VI}O_4)(PO_4)_2$ (M^{III} = Fe, Sc; M^{VI} = Mo, W), novel members of the lagbeinite-related family: synthesis, structure, and magnetic properties. *Inorg. Chem.* 2012, *51*, 1380–1385.
52. Domenges B., McGuire N., O'Keeffe M. Bond lengths and valences in tungsten oxides. *J. Solid State Chem.* 1985, *56*, 94–100.
53. Donnay G., Allmann R. How to recognize O^{2-}, OH^-, and H_2O in crystal structures determined by X-rays. *Am. Mineral.: J. Earth Planet. Mater.* 1970, *55*, 1003–1015.
54. Baltrusaitis J., Mendoza-Sanchez B., Fernandez V., Veenstra R., Dukstiene N., Roberts A., Fairley N. Generalized molybdenum oxide surface chemical state XPS determination via informed amorphous sample model. *Appl. Surf. Sci.* 2015, *326*, 151–161.
55. Vasilopoulou M., Douvas A. M., Georgiadou D. G., Palilis L. C., Kennou S., Sygellou L., Soultati A., Kostis I., Papadimitropoulos G., Davazoglou D., Argitis P. The influence of hydrogenation and oxygen vacancies on molybdenum oxides work function and gap states for application in organic optoelectronics. *J. Am. Chem. Soc.* 2012, *134*, 16178–16187.
56. Scanlon D. O., Watson G. W., Payne D. J., Atkinson G. R., Egdell R. G., Law D. S. L. Theoretical and experimental study of the electronic structures of MoO_3 and MoO_2. *J. Phys. Chem. C* 2010, *114*, 4636–4645.
57. Yan J., Wang T., Wu G., Dai W., Guan N., Li L., Gong J. Tungsten oxide single crystal nanosheets for enhanced multichannel solar light harvesting. *Adv. Mater*. 2015, *27*, 1580–1586.
58. Lisnyak V., Slobodyanik M., Sudavtsova V. Interactions in the $LiPO_3$–MoO_3, $NaPO_3$–MoO_3, and KPO_3–MoO_3 systems. *Powder Metall. Met. Ceram.* 2000, *39*, 139–145.
59. Di Benedetto F., Andreozzi G., Bernardini G., Borgheresi M., Caneschi A., Cipriani C., Gatteschi D., Romanelli M. Short-range order of Fe^{2+} in sphalerite by ^{57}Fe Mössbauer spectroscopy and magnetic susceptibility. *Phys. Chem. Miner.* 2005, *32*, 339–348.
60. Russell D. D., Neer A. J., Melot B. C., Derakhshan S. Long-range antiferromagnetic ordering in B-site ordered double perovskite Ca_2ScOsO_6. *Inorg. Chem.* 2016, *55*, 2240–2245.

61. Wolf S., Awschalom D., Buhrman R., Daughton J., von Molnár v. S., Roukes M., Chtchelkanova A. Y., Treger D. Spintronics: a spin-based electronics vision for the future. *Science* 2001, *294*, 1488–1495.
62. Tordjman I., Masse E., Guitel J. Structure cristalline du monophosphate $KTiPO_5$. *Z. Kristallogr.* 1974, *139*, 103–115.
63. Peuchert U., Bohatý L., Fröhlich R. $K_2NiWO_2(PO_4)_2$: a new structure type related to $KTiOPO_4$ (KTP). *Acta Crystallogr. C Struct. Chem.* 1995, *51*, 1719–1721.
64. Peuchert U., Bohatý L., Schreuer J. The triclinic room-temperature modification of $K_2MgWO_2(PO_4)_2$. *Acta Crystallogr. C Struct. Chem.* 1997, *53*, 11–14.
65. Babaryk A., Zatovsky I., Baumer V., Slobodyanik N., Nagorny P., Shishkin O. Novel KTP-like complex phosphates $KM^{II}_{0.33}Nb_{0.67}PO_5$ (M^{II}: Mn, Co). *J. Solid State Chem.* 2007, *180*, 1990–1997.
66. Domengès B., Hervieu M., Raveau B., O'Keeffe M. Potassium monophosphate tungsten bronzes with hexagonal tunnels, $K_x(PO_2)_4(WO_3)_{2m}$: X-ray diffraction and HREM study. *J. Solid State Chem.* 1988, *72*, 155–172.
67. Salje E., Carley A., Roberts M. The effect of reduction and temperature on the electronic core levels of tungsten and molybdenum in WO_3 and $W_xMo_{1-x}O_3$—a photoelectron spectroscopic study. *J. Solid State Chem.* 1979, *29*, 237–251.
68. Goudjil M., Lepore G. O., Bindi L., Mugnaioli E., Baroni T., Mezaoui D., Bonazzi P. Synthesis and characterization of $AsO[(W, Mo)O_3]_{13}$, a new (6)-intergrowth tungsten bronze (ITB). *J. Solid State Chem.* 2023, *322*, 123987.

Supplementary Material: The article contains supplementary material (https://doi.org/10.1515/zkri-2023-0027).